The 2017 Mega-Fires in Central Chile: Impacts on Regional Atmospheric Composition and Meteorology Assessed from Satellite Data and Chemistry-Transport Modeling

Rémy Lapere, Sylvain Mailler, Laurent Menut

atmosphere

MDPI

Article

The 2017 Mega-Fires in Central Chile: Impacts on Regional Atmospheric Composition and Meteorology Assessed from Satellite Data and Chemistry-Transport Modeling

Rémy Lapere [1,*], Sylvain Mailler [1,2] and Laurent Menut [1]

[1] Laboratoire de Météorologie Dynamique, IPSL, École Polytechnique, Institut Polytechnique de Paris, ENS, Université PSL, Sorbonne Université, CNRS, 91128 Palaiseau, France; sylvain.mailler@lmd.ipsl.fr (S.M.); laurent.menut@lmd.ipsl.fr (L.M.)
[2] École des Ponts, Université Paris-Est, 77455 Champs-sur-Marne, France
* Correspondence: remy.lapere@lmd.ipsl.fr

Abstract: In January 2017, historic forest fires occurred in south-central Chile. Although their causes and consequences on health and ecosystems were studied, little is known about their atmospheric effects. Based on chemistry-transport modeling with WRF-CHIMERE, the impact of the 2017 Chilean mega-fires on regional atmospheric composition, and the associated meteorological feedback, are investigated. Fire emissions are found to increase pollutants surface concentration in the capital city, Santiago, by +150% (+30 µg/m^3) for $PM_{2.5}$ and +50% (+200 ppb) for CO on average during the event. Satellite observations show an intense plume extending over 2000 km, well reproduced by the simulations, with Aerosol Optical Depth at 550 nm as high as 4 on average during the days of fire activity, as well as dense columns of CO and O_3. In addition to affecting atmospheric composition, meteorology is also modified through aerosol direct and indirect effects, with a decrease in surface radiation by up to 100 W/m^2 on average, leading to reductions in surface temperatures by 1 K and mixing layer heights over land by 100 m, and a significant increase in cloud optical depth along the plume. Large deposition fluxes of pollutants over land, the Pacific ocean and the Andes cordillera are found, signaling potential damages to remote ecosystems.

Keywords: biomass burning; WRF-CHIMERE; air pollution; on-line coupling; aerosol feedback; central Chile

Citation: Lapere, R.; Mailler, S.; Menut, L. The 2017 Mega-Fires in Central Chile: Impacts on Regional Atmospheric Composition and Meteorology Assessed from Satellite Data and Chemistry-Transport Modeling. *Atmosphere* **2021**, *12*, 344. https://doi.org/10.3390/atmos12030344

Academic Editor: Yoshiteru Iinuma

Received: 3 February 2021
Accepted: 3 March 2021
Published: 6 March 2021

1. Introduction

In summertime, air quality in central Chile (32°–38° S, 70°–73° W) is mostly affected by ozone (O_3) pollution in urban and sub-urban areas, with hourly maxima reaching typically up to 55 ppb in downtown Santiago [1]. This phenomenon originates in the combination of large emissions of nitrogen oxides (NO_x) from traffic and industry (typically around 60 ppb daily maxima in downtown Santiago), volatile organic compounds (VOCs) from anthropogenic sources and vegetation (typically around 70 ppb on average in downtown Santiago), with increased photo-chemistry [1,2]. The latter is made possible by long days and intense solar radiation. On the contrary, particulate matter (PM_{10}) pollution is usually lesser than in wintertime, due to less residential heating and hence less wood burning emissions of fine particulate matter ($PM_{2.5}$), together with deeper mixing layers diluting pollutants to a greater extent [2]. However, PM concentrations can sporadically reach or exceed wintertime levels for a few days in summertime, in association with massive forest fires in the region [3]. The production and transport of O_3 by these events also exacerbate air pollution in the affected urban areas [4].

The nature of gas and particulate emissions from forest fires varies depending on the burned species, but a subset of key pollutants are dominant and common to most fires, e.g., [5]. Greenhouse gases such as CO_2, CH_4 and N_2O find a significant part of their

worldwide emissions originating from forest fires. As is the case for BC and primary organic aerosols, for which biomass burning is believed to be the main source of emission globally. Other gaseous pollutants such as CO, NO_x and VOCs are also part of the key emitted species during forest fires. NO_x and VOCs undergo photochemistry right after emissions in the smoke plume, under daylight conditions, leading to the production of secondary pollutants such as O_3, which has impacts on plants productivity and threatens human health [6,7]. The increase in fine particulate matter concentrations from the transport of fire emissions to remote and urban areas also raises concerns regarding respiratory issues for human beings [8]. Acidic aerosols such as sulfuric acid (H_2SO_4) similarly generate pulmonary inflammations when inhaled [9]. In this study, analyses will focus on a selection of pollutants based on their level of harmfulness to human health, although many others could be relevant to look at.

Central Chile is characterized by a temperate Mediterranean climate so that wildfires occur every year in summertime although their magnitude is variable. Since the 1970's, forest fires in the region have been continuously growing in number and affected surface area, from 2000 fires per year corresponding to a 350 km^2 burned area for the period 1970–1979 on average to a mean 6000 fires and 1180 km^2 for the 2010–2019 period [10]. Multi-factorial changes underlie this evolution such as climate, biogeography, land use, and fire management [11–13]. In particular, the recent mega-drought recorded in central Chile aggravated the hydrological deficit in the region and partly explains the exceptional severity of fires observed over the last decade in the region [14–16].

In late January 2017, a record-breaking biomass burning event started in south-central Chile, destroying more than 5000 km^2 of plantations, native forests and shrublands in a few days. Although the number of wildfires observed in summer 2016/2017 is close to the decadal average, the total burned area is more than 5 times larger than any other year [10], hence their designation as mega-fires. The associated emissions and atmospheric transport of O_3 and PM_{10} affected air quality over most of the region and as far North as Santiago, the capital city, with significantly increased concentrations recorded throughout the air quality monitoring networks [3]. A wide range of social, economic, and environmental impacts result from these fires [17,18], in addition to an estimated 76 premature human deaths and 209 additional hospital admissions for respiratory conditions in the region [13]. To date, studies investigating the atmospheric impact of the 2017 fires rely on local measurements and satellite data analysis rather than modeling, which does not provide a comprehensive, spatially continuous analysis nor permits a scenario approach regarding atmospheric composition modifications induced by the 2017 mega-fires.

Chemistry-transport modeling (CTM) offers a solution to cope with such limitations, hence the extensive use of CTM scenario approaches to describe and assess the transport and impact of biomass burning emissions on atmospheric composition at the global, e.g., [19–21] and regional scale, e.g., [22–24]. In particular, the CHIMERE model [25] is extensively used for the study of atmospheric impacts of large biomass burning events in several areas of the world, with examples of application in Africa [26], Russia [27–29], and the Mediterranean [30–32].

Given the forecast increasing frequency of summertime droughts in the region for the years to come, identifying the climate feedback linked to biomass burning in central Chile is of significant importance. Examples of such feedback arise throughout the world. In the long run the radiative impact of aerosols emitted by biomass burning over the Amazon rainforest is found to improve the net primary productivity of biomass located downwind, due to changes in the more scattered nature of the light reaching the canopy, which in turn induces modifications in biochemical processes [33]. In South Africa, a Niña-like climate response to biomass burning is found, affecting the Walker circulation in the tropical Pacific through atmospheric teleconnections [34]. In the Southeast Atlantic region, biomass burning aerosols create a cyclonic anomaly over the ocean but enhance tropospheric stability over the continent [35]. Russian wildfires in summer 2010 decreased solar radiation significantly for a few days, resulting in a surface cooling of the region contributing to

stabilize and shallow the boundary layer, the latter leading to an increase in surface PM_{10} concentrations [28]. However, despite the 2017 mega-fires in Chile representing a major biomass burning event, the associated climate feedback is not known.

In this context, the present work aims to study and provide insight on the effects on atmospheric composition and meteorology of the 2017 mega-fires in central Chile. To do so, chemistry-transport modeling with WRF-CHIMERE is used, in fully coupled mode, to perform a sensitivity analysis to the fire emissions. Section 2 describes the data used and the modeling methodology adopted for the chemistry-transport simulations. Performance of the simulation compared to satellite data and local measurements, impacts on air quality and meteorological feedback are presented in Section 3. Section 4 discusses the findings and Section 5 elaborates on the conclusions of this work.

2. Materials and Methods

The adequacy of the simulations performed using the WRF-CHIMERE chemistry-transport model is assessed by comparison to surface measurements and satellite data, which are presented hereafter. The model setup and configuration as well as the fire emissions parameterization are also described here.

2.1. Observational Data

Time series of hourly measurements of atmospheric pollutants surface concentrations in Santiago are provided by the Chilean automated air quality monitoring network named SINCA (for spanish Sistema de Información Nacional de Calidad del Aire—https://sinca.mma.gob.cl/index.php/region/index/id/M (accessed on 1 October 2020)). Local measurements of Aerosol Optical Depth (AOD) and Single-Scattering Albedo (SSA) are extracted from the Santiago Beauchef station of the Aerosol Robotic Network (AERONET [36]—https://aeronet.gsfc.nasa.gov/ (accessed on 1 October 2020)). AOD at the regional scale is taken from MODIS Terra (http://dx.doi.org/10.5067/MODIS/MOD04_L2.061 (accessed on 1 October 2020)) and Aqua (http://dx.doi.org/10.5067/MODIS/MYD04_L2.061 (accessed on 1 October 2020)) level 2 aerosol products. Lidar satellite cross sections are taken from the CALIOP Lidar Level 2 Vertical Feature Mask Data, V4-20 (https://doi.org/10.5067/CALIOP/CALIPSO/LID_L2_VFM-STANDARD-V4-20 (accessed on 1 October 2020)) onboard the CALIPSO satellite. Carbon monoxide (CO) total column and O_3 tropospheric column satellite observations are taken from the IASI level 2 products [37].

2.2. Modeling Setup

The simulation domain comprises central and south-central Chile, between 15° S to 42° S and 63° W to 86° W (white domain in Figure 1b), at the 15 km spatial resolution. On the vertical, 30 levels are used up to the pressure of 300 hPa. CHIMERE v2020r1 is used, in fully coupled mode, integrating aerosols direct and indirect effects. CHIMERE is a Eulerian 3-dimensional regional Chemistry-Transport Model, able to reproduce gas-phase chemistry, aerosols formation, transport and deposition [25,38]. The v2020r1 version used in this work also provides a full coupling with the Weather Research and Forecasting (WRF) mesoscale numerical weather model from the US National Center for Atmospheric Research [39].

The simulated period is 15 to 31 January 2017, preceded by a spin-up period from 1 to 14 January 2017. Temperature anomalies and wind fields during the most intense fire period are described in Figure 1a, showing a large positive anomaly in surface temperature favoring the development of the fires, along with strong southerlies near the coast of central Chile that prefigure the general shape of the smoke plume. Parameterizations and schemes choices for CHIMERE and WRF are shown in Table A1. Fire emissions are extracted from the Copernicus Atmosphere Monitoring Service (CAMS) Global Fire Assimilation System daily data sets [40] and adapted to the CHIMERE format (see Section 2.2.1). Emissions of CO for this fire event reach up to several hundreds tons per day per grid point (Figure 1b), with more than 10 $t/day/km^2$ for the most affected locations. Anthropogenic emissions are

based on the HTAP v2.2 inventory [41], downscaled and split down in time to hourly rates following the methodology of [42]. Initial and boundary conditions rely on the NCEP FNL analysis data sets, with a 1° by 1° spatial resolution and 6-hour temporal resolution, from the Global Forecast System [43]. Land-use and orography are extracted from the modified IGBP MODIS 20-category database with 30 s resolution [44].

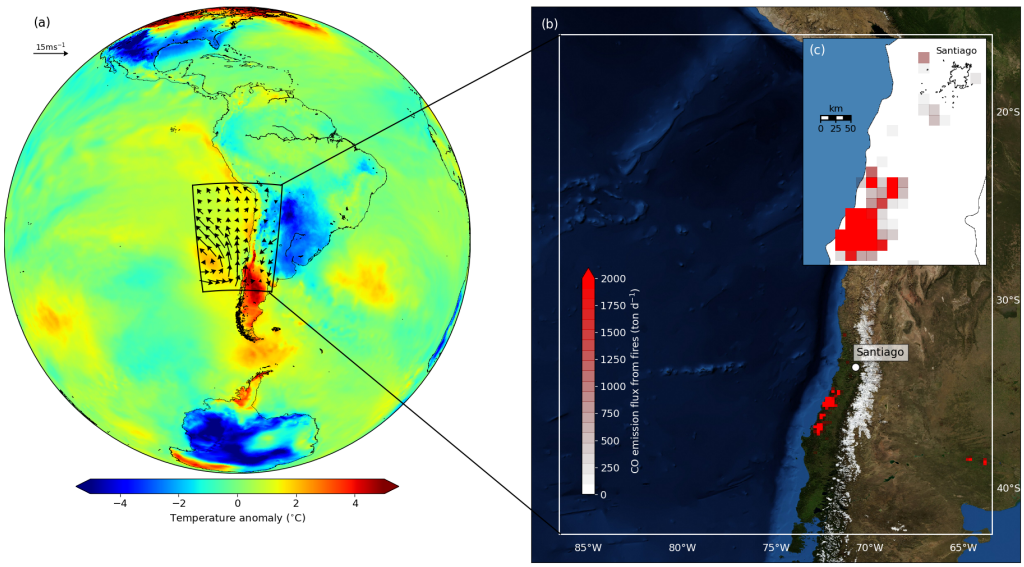

Figure 1. (**a**) Temperature anomaly between 25 and 29 January w.r.t. January 2017 average, and associated mean wind field. Data from ERA5 hourly surface reanalyses [45]. (**b**) Simulation domain (white boundaries) and CO emissions from the main fire areas on 29 January. Emission data from CAMS GFAS [40] pre-processed for CHIMERE. Map background layer: Imagery World 2D, ©2009 ESRI. (**c**) Zoom on the region of Santiago.

A first simulation is performed without considering emissions of pollutants from the fires (hereafter "control case"), and a second one including these emissions (hereafter "fire case"), so as to be able to perform a sensitivity analysis and isolate the effects stemming from the fire emissions. In the control case, all fire emissions are switched off, regardless of their location and magnitude, even during spin-up, as if the model were oblivious to fires.

2.2.1. Fire Emissions Parameterization

Emission rates of gases and particulate matter from fires are extracted from the CAMS GFAS daily emissions product and spatially downscaled to our simulation domain. A parameterized diurnal cycle is applied, with a daytime increase in emission rates until early afternoon (maximum at 16:00 UTC i.e., 13:00 LT) and low emission rates during nighttime (Figure A1a), consistently with what is usually observed for mid-latitude wildfires [30,46].

The vertical parameterization is similar to what is carried out in [26]. Fire emissions are injected between ground level and the injection height H_p which is computed after the methodology of [47] as Equation (1):

$$H_p = \alpha H_{ABL} + \beta \left(\frac{P_f}{P_{f0}}\right)^{\gamma} \exp\left(-\frac{\delta N_{FT}^2}{N_0^2}\right) \quad (1)$$

where α = 0.24 and H_{ABL} is the atmospheric boundary layer (ABL) height, so that the first term represents the fraction of the ABL that is passed "freely", β = 170 m, P_f and P_{f0} are the fire radiative power (FRP) and reference FRP (10^6 W), respectively, γ = 0.35, δ = 0.6, and N_{FT}^2 and N_0^2 are the Brunt-Väisälä frequency of the free troposphere and of reference ($2.5 \times 10^{-4}\,s^{-2}$), respectively. The second term hence corresponds to the available convective potential energy diagnosed based on the FRP. NB: P_f is empirically corrected according to [48] as $P_f^* = P_f \times \sqrt{H_p/1500}$.

The injection profile between the surface and H_p follows a K_z-like shape based on the approach from [48]. The emission factor (EF) for a given altitude z is expressed as Equation (2):

$$\begin{cases} \text{if} \quad z/H_p \leq 1, EF(z) = z(1 - z/H_p)^2 \\ \text{if} \quad z/H_p > 1, EF(z) = 0 \end{cases} \tag{2}$$

In our simulation this corresponds to emissions being distributed throughout the mixing layer with a maximum emission rate typically around 500 m above ground level, i.e., about halfway through the ABL. Figure A1a shows an example of diurnal cycle and vertical profile for January 29 at a strong emission grid point.

Results are expected to be sensitive to these parameterization choices: the choice of diurnal distribution of emissions affects the injection height given its dependence on meteorological conditions. In turn, the simulated transport depends on this injection altitude [31]. We acknowledge this source of uncertainty, although our modeling choices correspond to proven performing configurations with CHIMERE in the literature. Besides, the continuation shows that the model reproduces adequately surface and satellite observations, strengthening confidence in these choices.

CO_2 and H_2O not being included in our emissions inventory, carbon monoxide (CO) is by far the dominant emitted species (81% of the molecules), followed by methane (CH_4—5%), organic carbon (OC—2%) and non speciated fine (PPM_fin) and coarse (PPM_coa) particulate matter (1.8 and 1.3% respectively). It is worth noting that despite its criticality regarding radiative effects, black carbon (BC) constitutes only a limited fraction (0.2%) of emissions (Figure A1b).

3. Results

3.1. Fires Impact on Atmospheric Composition

In this section, the adequacy of the model in reproducing the observed changes in atmospheric composition due to the fire events is assessed. A quantitative estimate of the fires emissions burden on air quality at the local and regional scales is then proposed.

3.1.1. In Santiago

Figure 2a shows the distribution of observed and simulated hourly concentrations of $PM_{2.5}$, PM_{10}, O_3 and CO at ground level over the SINCA network in Santiago, during the intense fire period of 22 to 30 January. Except for O_3, the control case simulation yields largely underestimated concentrations, confirming the significant transport of biomass burning pollutants towards Santiago during the 2017 event, as was inferred from statistical analyses of observations in [3]. In the fire case, simulated concentrations are much closer to observations, especially for $PM_{2.5}$ and CO although the spread is larger in the simulation. The discrepancy between the mean and median can be accounted for by the generation of spikes with excessive intensity in the model, while the observed distribution shows limited skewness. Apart from skewness, the distribution quartiles are adequately reproduced by the model for these two pollutants.

Contrary to $PM_{2.5}$, PM_{10} is significantly underestimated by the model, even in the fire case, meaning the coarse fraction of particulate matter is not adequately emitted and/or transported. Although the model and observations are consistent for average PM_{10} surface concentration during the event (driven by intense peaks like for $PM_{2.5}$), the distribution is shifted toward lower values in the simulation. The discrepancy comes from a negative bias in the model even before the fire event. For the period preceding 22 January, i.e., without the influence of fires in Santiago, $PM_{2.5}$ is consistently reproduced by the model in the capital city (not shown here), but the coarse fraction of PM (PM_{10}-$PM_{2.5}$) is significantly underestimated: between 14 and 22 January, observations over the automated network of Santiago recorded a $PM_{2.5}/PM_{10}$ ratio of 0.4 on average, while the model yields 0.7 (not shown here). The underestimation of the coarse fraction of PM can stem from either too low emissions of coarse particles in the HTAP anthropogenic emissions inventory, or excess

dry deposition as (PM_{10}-$PM_{2.5}$) are substantially more deposited than $PM_{2.5}$ due to their greater mass. The latter point is sensitive to the choice of the deposition scheme, sometimes resulting in significantly different fluxes, e.g., [49]. However, emissions of aerosols by fires are usually mostly found in fine mode as is consistently shown both by the simulations and measurements: when the fire event starts, the $PM_{2.5}/PM_{10}$ ratio increases in both the model and observations, to around 0.8 and 0.6, respectively, (not shown here). Figure A2b also illustrates the dominance of fine mode aerosols transported from the fires. The lesser performance for PM_{10} thus does not jeopardize the present analysis regarding the influence of fires on atmospheric composition in Santiago, as it is mostly expected to affect the fine fraction of PM, which is well reproduced.

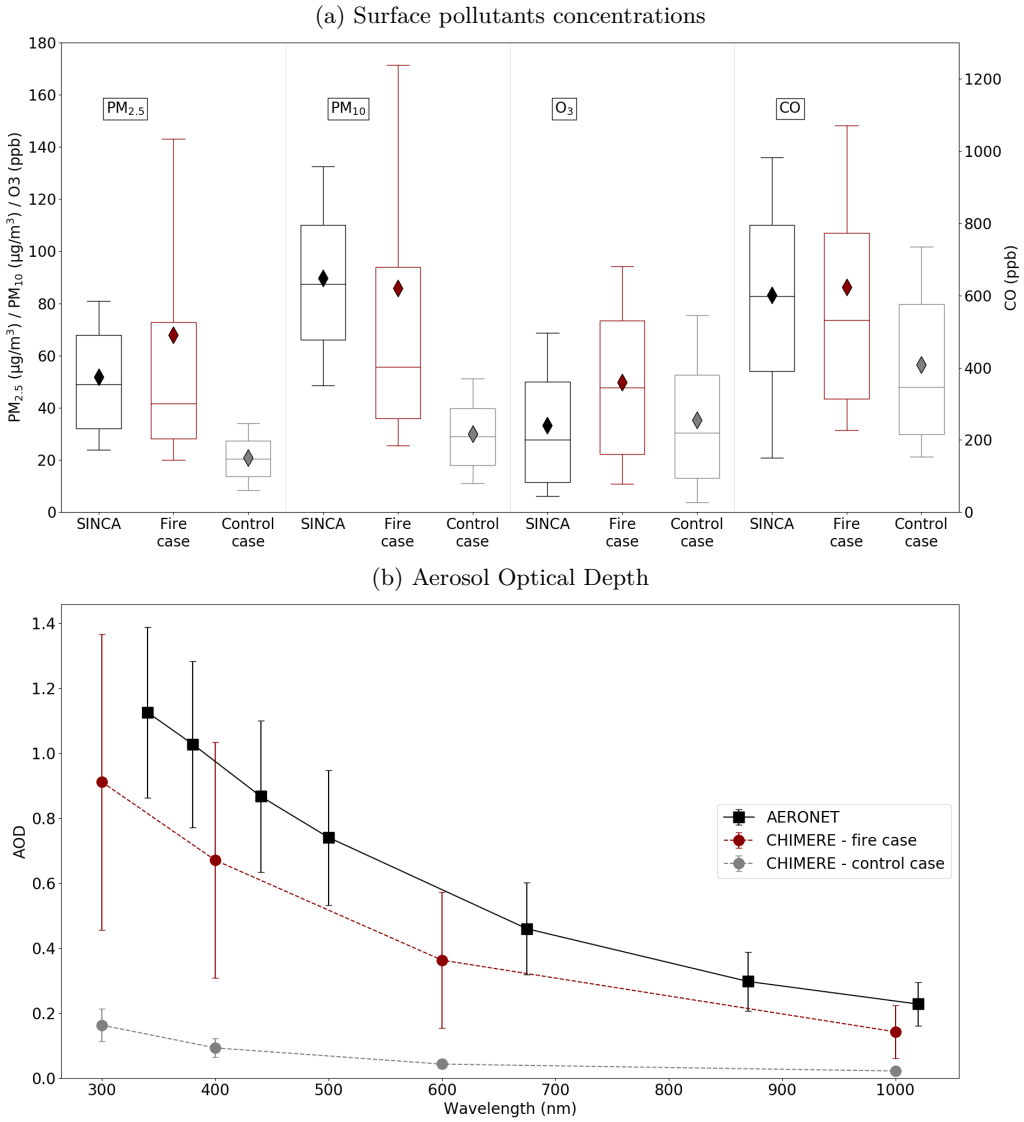

Figure 2. (**a**) Observed (black), and modeled (fire case in red, control case in gray) distribution of surface pollutants hourly concentrations in Santiago between 22 and 30 January. Distribution over 9 stations of the SINCA network (Parque O'Higgins, Las Condes, Independencia, Puente Alto, Pudahuel, La Florida, El Bosque, Cerrillos, Quilicura). Boxes show the median and first and third quartile, whiskers show 10% and 90% percentiles, diamonds show the mean. (**b**) AOD distribution by wavelength for the period 22 to 30 January for Santiago Beauchef AERONET station (same color code). Whiskers show one standard deviation.

For O_3, the simulations show an increase of mixing ratio by more than 10 ppb on average in the fire case compared to the control, which is consistent with the findings of [4] that showed significant O_3 transport to Santiago during the 2014 fires. However, the model is positively biased as the control case matches the observations while the fire case yields mixing ratios well above. Given the non-linearity of O_3 chemistry such a discrepancy can come from several uncertainty sources and does not allow to extract a quantitative estimate of the excess concentrations attributable to fires.

AOD in downtown Santiago also features a clear change in the signal when fire emissions are included (Figure 2b). During the days of strong fire intensity the observed AOD at 380 nm reaches elevated values as high as 1.5 on the daily average and up to 3 for one hour. Such levels are even higher than what is usually observed in wintertime when emissions from wood burning for residential heating strongly increase the aerosol load over the Metropolitan Area. Before the fire period, the usual summertime AOD daily mean of around 0.25 is recorded (not shown here). For the period between 22 and 30 January, in the control case, AOD at all wavelengths show average values between 0.01 and 0.2, while observations and simulation in the fire case indicate AOD around 1 at 300 nm and 0.3 at 1000 nm. The model shows a small negative bias and more spread AOD distribution compared to observations from AERONET, at all wavelengths (mean bias of -0.12 and Pearson correlation coefficient of 0.45 at 340 nm on the hourly time series). For the larger wavelengths, the underestimation is consistent with the previous statement that the simulation is negatively biased regarding the coarse fraction of PM, even in the control case preceding the fire events. Furthermore, Santiago being near the edge of the main dense plume, the simulated signal at this grid point is tangential so that a small error in the transport or the magnitude of emissions will result in a relatively large bias there, which partly explains degraded performance, although standard deviations still overlap for every wavelength. Unfortunately, other AERONET stations in south-central Chile did not record any data for the period so that other comparisons are prevented.

A comparison of the volume size distribution of aerosols before and during the fires (Figure A2b) shows that both fine (diameter smaller than 2.5 µm) and coarse (diameter between 2.5 and 10 µm) mode are reinforced by the smoke plume, with a significantly larger increase in the fine mode, tied to the transport of BC and OC. In parallel, the SSA becomes more spread across wavelengths when fires start to kick in, with its values decreasing in the longer wavelengths (Figure A2a). Again, this relates to BC and OC being brought over to Santiago as these two species have SSA of around 0.5 and 0.8, respectively, when emitted from biomass burning [50], hence driving down the scattering efficiency compared to absorption. Again, fires affect aerosols properties measured in Santiago.

In summary, simulations and observations both point towards a large contribution of fire emissions to air pollution and modification of atmospheric composition in Santiago during the 2017 event. The model allows to quantify the burden induced by the transport of fire-emitted pollutants towards Santiago on $PM_{2.5}$ and CO concentrations in the capital city, as well as AOD, with excess concentrations of 30 $\mu g/m^3$ (+150%) and 200 ppb (+50%), respectively, and an increase of AOD by a factor between 6 and 8 for all wavelengths, on average for the period 22 to 30 January, and a peak at 2.5 in AOD at 500 nm recorded by AERONET during the event. However, the degraded performance on O_3 and PM_{10} in the capital city only allows for qualitative conclusions for these pollutants.

3.1.2. At the Regional Scale from Satellites

Figure 3 compares satellite observations from IASI (Metop-b CO total column and O_3 partial column) and MODIS (AOD at 550 nm) to the corresponding simulated variables in CHIMERE. The satellite panels are gridded at 0.5° resolution and composited averaging all available data for each grid point over the period 25 to 29 January of high fire intensity. Simulation values are extracted at the corresponding passage times of Metop-b and Terra/Aqua, so as to recreate what the satellites would see if they observed the model.

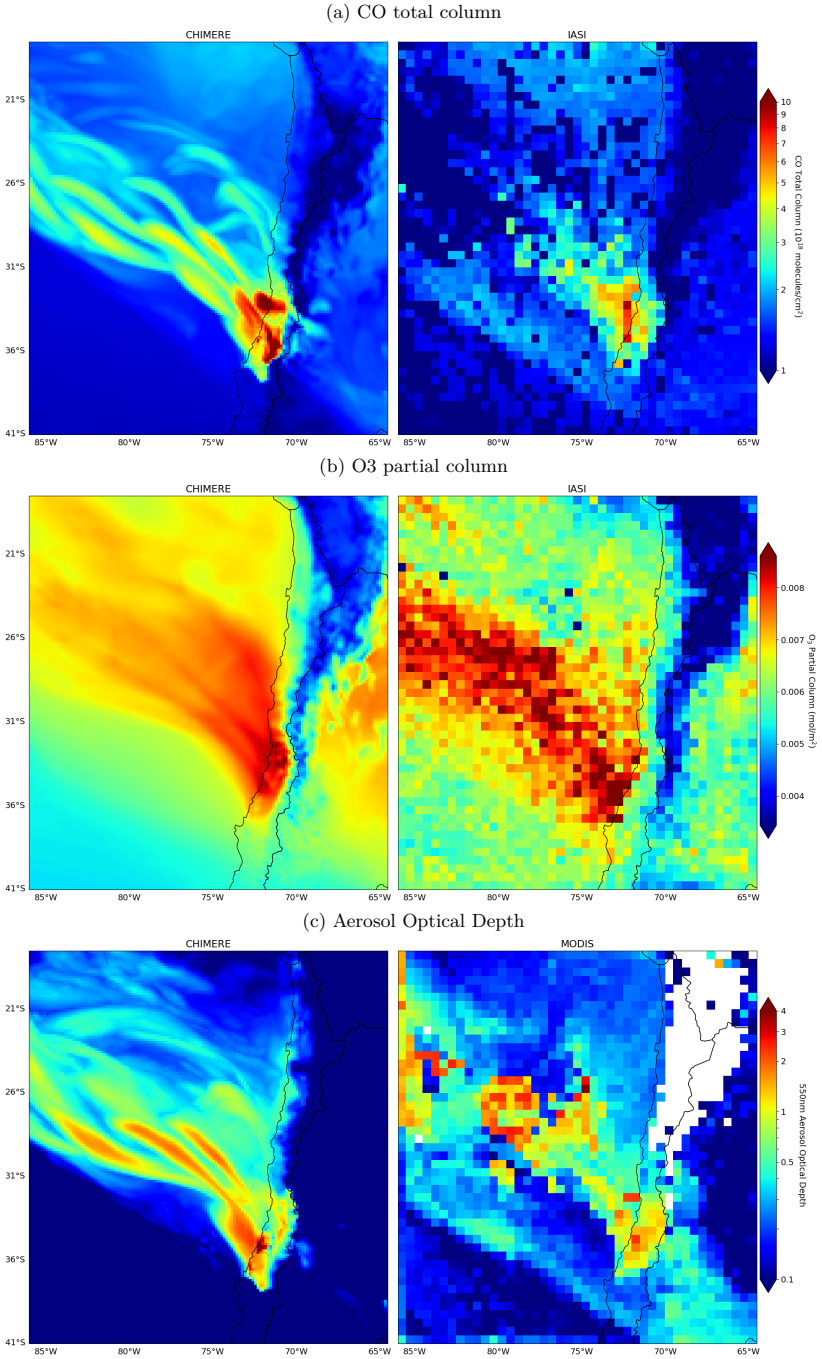

Figure 3. (**a**) CO total column composite as simulated by CHIMERE (**left**) and recorded by IASI Metop-b (**right**). (**b**) O_3 tropospheric column between 0 and 8 km altitudes composite as simulated by CHIMERE (**left**) and recorded by IASI Metop-b. (**c**) 550 nm Aerosol Optical Depth composite as simulated by CHIMERE (**left**) and recorded by MODIS Terra and Aqua level 2 products (**right**). All panels show composited averages for the period 25 to 29 January.

The simulation yields a CO total column slightly more intense than IASI near the emission area and a more extended plume. These discrepancies come from the discrete and partial nature of the data from IASI that feature many indeterminate values for the area and the period. However the shape of the plume and magnitude of the total column are well in accordance between measurements and modeling, showing a dense CO load up to 80° W and a blocking effect by the Andes cordillera towards the east (Figure 3a). O_3 partial columns also compare quite well in terms of the shape and extent of the plume, while the model mostly underestimates the O_3 load by a few percents. Again, the scarcity

of valid measurements from satellite data leads to a bias where some grid points only have one value for IASI while CHIMERE shows an average for the period, hence shaving more the peak values. Nevertheless the magnitudes are still in good agreement, and both show an O_3 plume extending diagonally northwestward across 15° of longitude and latitude, i.e., around 2000 km (Figure 3b). Similar observations can be made for the comparison with MODIS data. The area of high intensity and downwind of the fires recorded AOD at 550 nm as high as 4 on average over the 5 days period (Figure 3c) and locally higher than 5 at a given point in time, suggesting significant direct radiative effects as explored later on in this work. Such AOD levels are comparable to what was recorded by MODIS during the fires in Australia in early 2020 and in Siberia in summer 2020 (see the NASA Worldview application for instance https://worldview.earthdata.nasa.gov (accessed on 1 October 2020)), stressing again the exceptional character of the 2017 Chilean fires studied here. In summary, the combination of all panels in Figure 3 shows the large extent and high density of the plume generated by the 2017 mega-fires and the good performance of the simulation in reproducing the emissions and horizontal transport of fire-emitted pollutants over the region for this event.

The Vertical Feature Mask (VFM) product of CALIOP provides information on the altitude and nature of dominant aerosols along vertical transects [51]. CHIMERE outputs from the fire case are transformed so as to recreate what CALIOP would see from that perspective if it observed the model, as shown in Figure 4 for 26 and 29 January in the morning. For these two transects, the vertical shape of the plume is consistent between satellite and model data, except for the nature of the high elevation plume between 35° S and 30° S on 29 January, where CALIOP sees mostly polluted dust with a bit of elevated smoke, while CHIMERE simulates only elevated smoke, according to the VFM classification. Given the biomass burning nature of the event, the simulation's output and CALIOP records both make sense in this regard. Generally speaking there is good agreement on the vertical transects compared here, giving confidence in the model's ability to reproduce the vertical distribution of pollutants. CALIOP and CHIMERE both consistently show that the plume of aerosols was injected as high as 6 km above ground, the highest altitudes being reached above the ocean, for the plume downwind of the main fire locations. On 26 January over land, both find the smoke plume getting vertically more extended as it moves northward, indicating a possible ramping effect of the topography along that direction, combined with a channeling effect of the Andes cordillera.

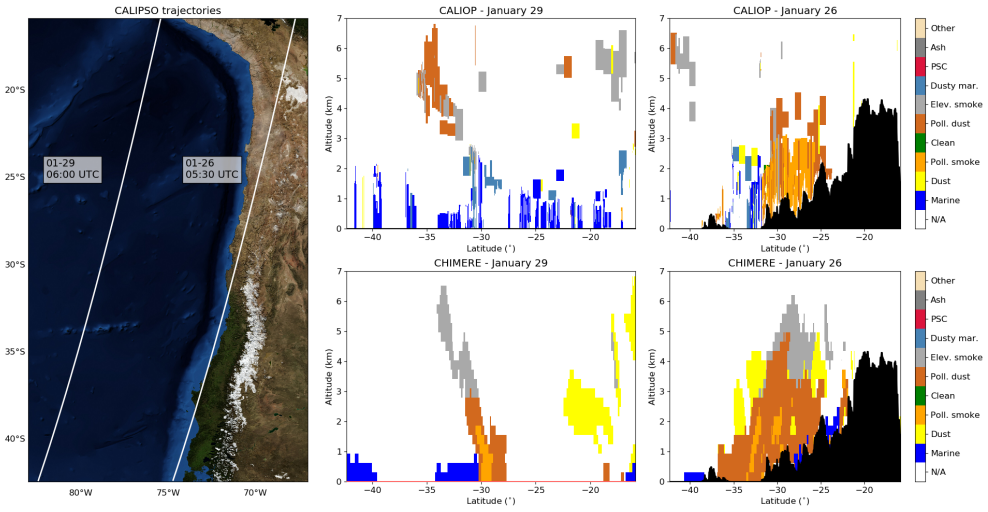

Figure 4. (**Left**) Trajectories of the CALIPSO legs for 26 and 29 January at 05:30 and 06:00 UTC, respectively, (white lines). Map background layer: Imagery World 2D, ©2009 ESRI. (**Middle** and **Right**) Vertical feature mask from CALIOP (top) and corresponding vertical feature mask extracted from CHIMERE for 26 and 29 January, respectively. Black filled contour shows terrain elevation along the transect.

A limitation to the previous comparison is the choice made for the translation from CHIMERE concentration fields into the VFM classification. The structure of the transect is somewhat sensitive to the mapping used between CALIOP optical indices and CHIMERE aerosol concentrations. In this work, an approach similar to [26] is adopted to establish the correspondence and cope with the difficulties raised in the literature regarding CALIOP's detection algorithm [52–54].

In addition to a description at the regional scale of different aspects of the pollutants plume emitted by the 2017 biomass burning event, the previous analysis provides confidence in the model behavior both on the horizontal and the vertical, over land and the ocean. This legitimates the impact analysis on air quality and meteorology over the region that is carried on later on in this work.

3.1.3. At the Regional Scale from the Model

Figure 5 shows the average excess surface concentration of CO, BC, O_3 and particle phase H_2SO_4 due to the fire activity, as well as two vertical transects (one along each main advection direction) of said concentrations, during the 2017 mega-fires peak intensity period (25 to 29 January). NB: In CHIMERE, 'particle phase H_2SO_4' is to be understood as 'sulfate aerosols', i.e., H_2SO_4 crystals and all sulfate in particle phase (ions, molecules, precipitates) deriving from the condensation of gas-phase H_2SO_4. The species considered are transported in significant amounts as far as 20° northward and 15° westward before vanishing or reaching the simulation domain boundaries. According to the vertical transects in Figure 5, the Andes act as a barrier, channeling pollutants on a meridional axis, and preventing their eastward dispersion, especially in the northern part of the cordillera where elevations are higher (transects (a) in Figure 5). In the south, summits are lower so that a fraction of the pollutants, particularly the gases, can travel above the mountains (a few ppb for O_3 and a few tens of ppb for CO). In that case, the Andes act as a ramp, injecting the pollutants higher up compared to the plume that goes westward over the ocean, in relation with mountain-valley circulation patterns governed by upslope winds during the afternoon. However, for fine particulate matter such as BC, even the lower Southern Andes act as an efficient barrier as the simulated concentrations near the summits are less than $1\,\mu g/m^3$.

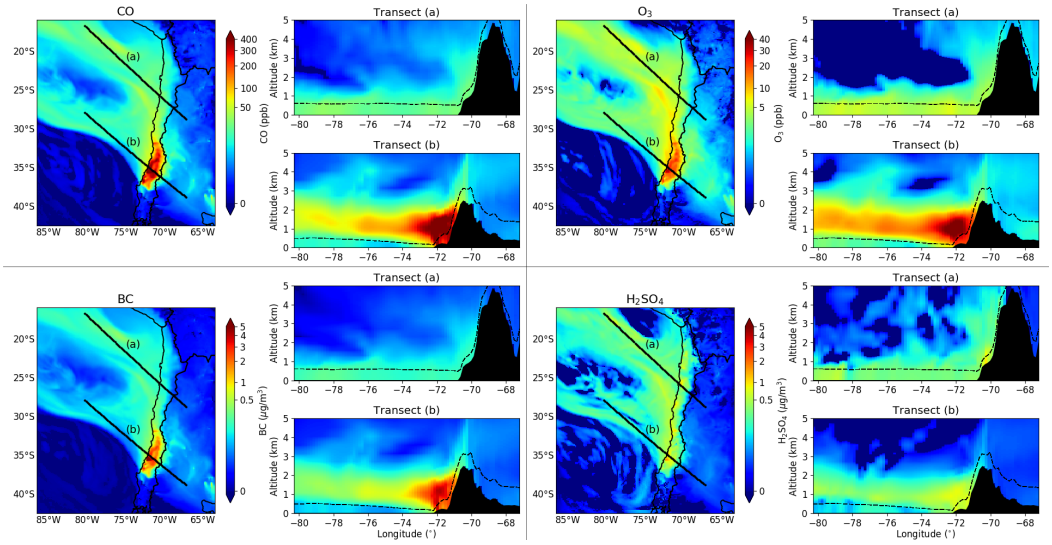

Figure 5. Excess concentrations of CO, O_3, BC and H_2SO_4 (particle phase) due to the contribution of fire emissions. Average for 25 to 29 January at the surface level and along two vertical transects. Each panel is composed of a map of surface concentrations (**left**), a northern transect along trajectory (a) shown in the surface map (**top right**), a southern transect along trajectory (b) shown in the surface map (**bottom right**). Black dashed line in the transects is the average mixing layer height along the transect. Black filled contours show terrain elevation.

The plume near the locations of higher fire intensity (transects (b) in Figure 5) is mainly contained in a layer between 1 km and 3 km altitude, above the mixing layer, rising steadily as it transports farther. Inside this plume, concentrations of CO, BC, O_3 and H_2SO_4 can reach values as high as a several hundreds ppb, tens of $\mu g/m^3$, several tens ppb and a few $\mu g/m^3$, respectively, with mean levels between100 and 1000 ppb, 1 and 10 $\mu g/m^3$, 10 to 50 ppb, and 0.5 to 1 $\mu g/m^3$, respectively. The other leg of the plume, in the north (transects (a) in Figure 5), is less dense and more homogeneous, mostly contained within the planetary boundary layer, except for the venting effect of the Andes that injects residual concentrations higher up and forms a secondary layer around 3500 m altitude near 72° W. It is worth noting that along this northern transect, O_3 above 2 km is slightly depleted in the fire case compared to the control case, by around 1 ppb on average. The main lower plume, where mixing ratios increase in the fire case is composed of O_3 formed close to the fires then advected, but in this depleted region, little O_3 is transported while simultaneously other gases such as CO or CH_4 reach this area. Although in minor quantities, the addition of these compounds slightly modifies the photochemical state of the atmosphere in this zone, reducing the availability of O_3 precursors, hence lowering the background mixing ratio. It is also interesting to see that the plume of H_2SO_4 is more homogeneously spread than the three other pollutants considered in Figure 5, without a sharp peak of concentrations near the fires location. This observation is consistent with the fact that the formation of H_2SO_4 (gas and particle phase) is favored in an ageing biomass burning plume compared to a fresh one, e.g., [55]. The conversion rate of its precursor SO_2 is determined by the hydroxyl radical (OH) concentration. However, OH is primarily consumed by NO_2, also emitted in large amounts by the fires, one order of magnitude faster than by SO_2 [56], hence leaving little OH available for the latter. Accordingly, the plume of HNO_3 observed in the simulation and formed by the reaction of NO_2 against OH, shows a large spike near the fires origin as is observed for BC or CO (not shown here), corroborating the dominance of consumption of OH by NO_2 over SO_2 near the fires origin. As a result, although SO_2 is liberated in larger quantities near the fires origin (the SO_2 plume is similar in shape to that of CO - not shown here), the ability of H_2SO_4 to form increases as the plume moves further away and NO_2 levels decrease, hence leaving more OH available. The consequent H_2SO_4 plume is thus more homogeneous as quantities of SO_2 decrease as the plume ages but available OH quantities increase simultaneously.

Figure 6 highlights significant deposition fluxes of the considered species throughout the fire event. BC is deposited in large amounts over land near the fires origin with up to more than 500 $\mu g/m^2$ in a few days. Fluxes of BC are also important over the Andes mountain range. H_2SO_4 deposition is mostly observed over the ocean, far from the Chilean coast, with up to more than 2 mg/m^2 in the area [30° S; 80° W–25° S; 85° W]. Over the ocean, we find that both BC and H_2SO_4 are dominantly deposited via wet processes, while dry deposition occurs mostly near the fires origin over land. For these two species, the scattered deposition pattern on the eastern side of the Andes north of the domain is artificial and due to a perturbation of precipitation in that region between the two simulation cases, and should not be attributed to the fire event as in this area dipoles of negative/positive changes in deposition cancel out eventually. O_3 is dominantly deposited over land, as its primary deposition process comes from the uptake by plant leaves. The model yields a total deposition of more than 50 mg/m^2 between 37° S and 32° S over the fires period for this pollutant. Possible impacts of the significant deposition fluxes of pollutants observed in Figure 6 associated with the particular locations they affect are further discussed in Section 4.

In summary, biomass burning emissions from the 2017 mega-fires induced a dramatic input of pollutants into the atmosphere, with effects on health and possibly on ocean water, crop yields and glaciers albedo. In addition to such environmental feedback, impact on the regional meteorology are also at stake, as described hereafter.

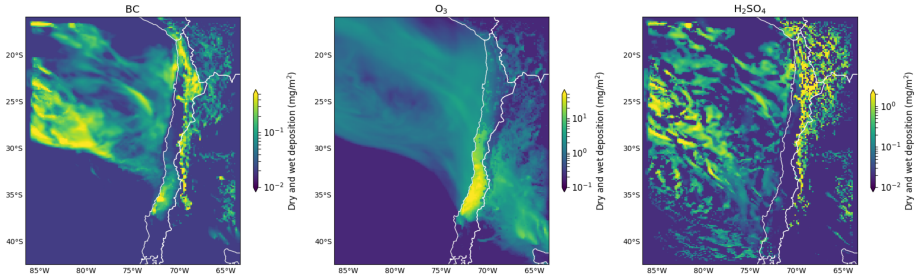

Figure 6. Accumulated deposition (dry+wet) of BC, O_3, and H_2SO_4 (particle phase) attributable to fires (fire-control) from 25 to 31 January. NB: deposition colormaps use a log scale.

3.2. Fires Impact on Meteorology

At the global scale, the atmospheric burden of gases and particles emitted by forest fires result in perturbations that have important consequences on climate. In particular, aerosols, especially light-absorbing particles, have a direct effect, scattering and absorbing solar radiation hence changing its nature and intensity when it reaches the ground. In addition to the modification of biogeochemical processes, this change in radiation affects temperature profiles and can in turn have an influence on atmospheric circulation. Indirect consequences of the release of such aerosols include the modification of the amount and properties of clouds, which has an impact on precipitation and albedo and thus radiation, entering a positive feedback loop [5]. These direct and indirect effects, although conceptually accessible, are complex and hard to measure and model, hence being one of the main uncertainties in climate projections according to [57]. Hereafter, we estimate the aforementioned effects attributable to the 2017 mega-fires on the regional climate of central Chile.

3.2.1. Indirect Effects

Satellite imagery during a day of the period of intense fires (27 January) shows the formation of clouds above the Pacific ocean, downwind of fires, along the coast of central Chile (Figure 7a). Given the mixed brown/white colors of the cloud cover recorded by MODIS, the aerosols found in the fire smoke plume likely play a role in its formation. This hypothesis is tested using the simulation's sensitivity analysis. For that particular day, CHIMERE is consistent with MODIS regarding the location of the main fires (red spots in Figure 7a,b), and produces a cloud cover comparable to that observed by MODIS, with denser clouds along the plume (red contour in Figure 7b). Averaged over three consecutive days (27–29 January), we find that most of the cloud cover is found over the ocean along the aerosols plume (Figure 7c). For that smoke-affected region, defined by the light brown filled contour in Figure 7c, the difference in distribution of hourly cloud cover, between the fire and control case, is shown in Figure 7d for the three days aforementioned and compared to a previous period featuring limited fire activity.

During that latter period, given the very limited fire activity, emission rates are close between the fire and control cases, so that meteorological fields should not change significantly from one simulation to another. However, small changes are observed in the cloud OD distribution, symmetrical to zero, that are induced by the slight perturbation in emissions, resulting in a slightly different state of the atmosphere, inducing an artificial displacement of clouds. During the fire days however, the cloud OD distribution is significantly shifted towards larger values in the fire case, indicating the thickening and creation of clouds due to the presence of fire-emitted aerosols acting as cloud condensation nuclei (CCN). Nevertheless, the simulated increase in cloud OD is significantly smaller than the average for the three days (up to 12 hourly in Figure 7d while the average is mostly above 20 in Figure 7c), so that according to the model, the cloud cover mostly preexists regardless of the presence of fires and is solely strengthened. This observation is further discussed in Section 4.

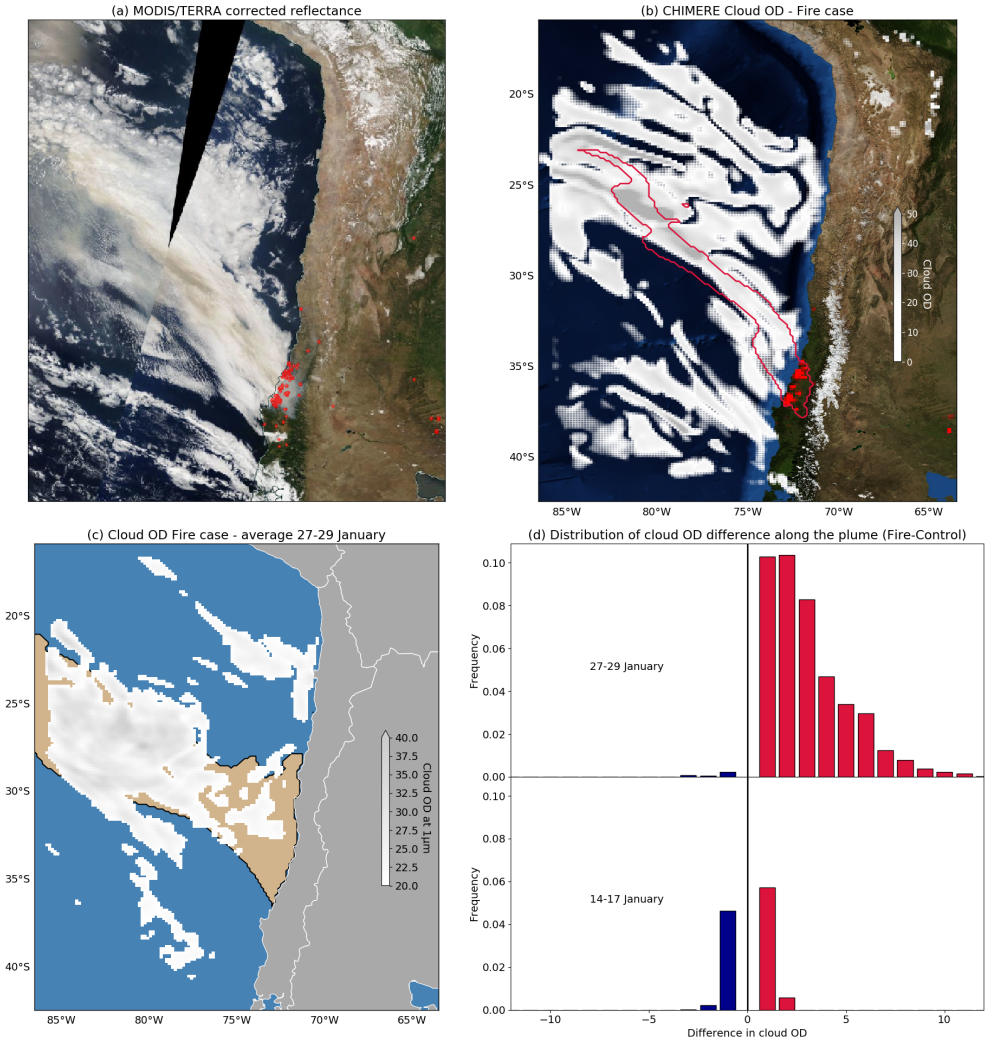

Figure 7. (**a**) Corrected reflectance product from MODIS/TERRA on 27 January provided by the NASA EOSDIS Worldview platform. Red spots show the fire and thermal anomalies as retrieved by MODIS. (**b**) CHIMERE simulated cloud OD at 1 µm at the passage time of MODIS on 27 January. Red spots correspond to the main emission sites at that time in the simulation. Red contour shows the shape of the aerosol plume originating from the fires. Map background layer: Imagery World 2D, ©2009 ESRI. (**c**) Cloud OD at 1 µm in the fire case averaged for 27 to 29 January (colormap). The light brown shade shows the extent of the PM plume originating from the fires. (**d**) Distribution of the cloud OD change in the fire case compared to the control case, over the region defined by the light brown shade in (**c**), for a fire period (27–29 January) and a non-fire period (14–17 January). NB: the central $[-0.5, 0.5]$ bin is removed for improved readability.

3.2.2. Combined Effects

In addition to the aforementioned indirect effects, direct effects superimpose, tied to radiation perturbation by the scattering and albedo effects of the particles themselves. In particular, under clear-sky conditions the addition of light-absorbing particles in the atmosphere reduces the downwelling solar radiation reaching the ground. The interaction between aerosols and radiation leads to rapid adjustments over land, which are even more marked with dark aerosols such as BC [58].

Figure 8a shows a large reduction, on average over four intense fire days, of ground shortwave radiation by up to more than 100 W/m^2 locally, especially over land near the fires origin and over the ocean in the region of denser cloud cover. A direct consequence over land is a decrease in surface air temperature by up to 1 K on average (Figure 8b). Over the ocean on the contrary, a slight warming is observed near the coast. The heat

capacity of the ocean is high, so that it has a strong thermal inertia. Thus, the response to the change in daytime radiation is limited, while at night the layer of aerosols yields back heat and traps outgoing radiation at the same time so that the ocean cools less than normally. All combined, this results in the observed surface air slight warming over the Pacific shore contrasting with the cooling over land. Similarly, the reduction in surface radiation limits the development of the planetary boundary layer, making it lower by up to 100 m over land on average over the period. In turn, this shallower mixing layer implies that pollutants are even more concentrated, since diluted in a smaller volume, hence evidencing a positive feedback loop. Furthermore, given the radiation-driven nature of surface winds in mountain environments, the decrease in solar energy reaching the ground leads to slightly lower wind speeds over the south-central Chilean land (Figure 8d). During daytime, the differential heating of air masses between plains and valleys usually gives rise to westerlies blowing towards the Andes. However, during the fire event, the lesser fraction of radiation reaching both environments prevents this phenomenon of mountain-valley circulation from happening, as would be the case during cloudy days [59]. Over the ocean no clear pattern is observed in this regard. Numerous small perturbation dipoles appear in Figure 8 especially far from the fire event. The displacement phenomenon mentioned previously is responsible for this noisy appearance.

The standard deviation associated with the mean effects presented in Figure 8, is generally speaking of the order of magnitude of the mean for the whole domain (not shown here). This indicates that the feedback is variable in time, with a large heterogeneity depending on the activity of the fires and with a strong diurnal cycle, although it is significant based on statistical tests.

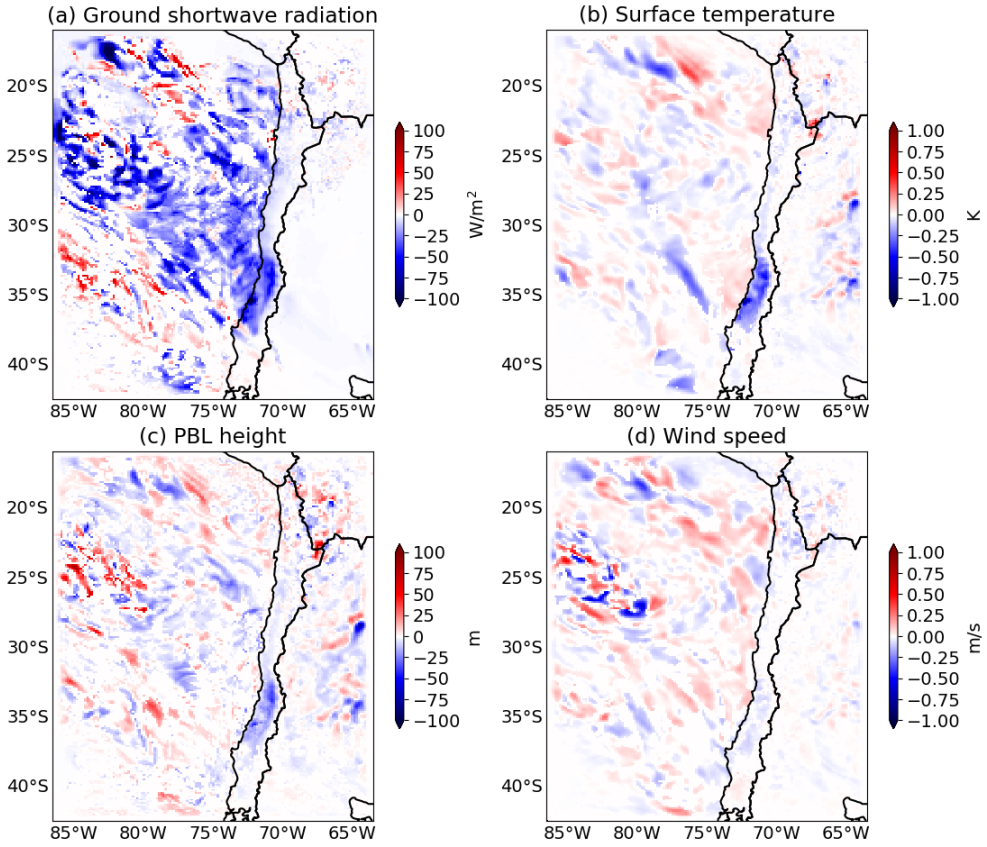

Figure 8. Effect of fire emissions on (**a**) surface shortwave radiation, (**b**) planetary boundary layer height, (**c**) surface air temperature, (**d**) 10m wind speed. Difference between the fire case and control case. Average for 26–29 January. Only grid points where the distribution of concentrations in the fire case is different than in the control case at the 99% level, based on a Wilcoxon test, are shown.

4. Discussion

Significant deposition of pollutants originating from fire emissions were observed in Figure 6, which potential environmental impacts are discussed hereafter. Although the effects of BC deposition on vegetation is still debated—partly fertilizing when deposited on the ground [60], partly detrimental when deposited on the leaves [61]—the large deposition fluxes at stake might be of importance. Such deposition also occurs on high altitude areas in the Andes, with possible impacts on glaciers albedo [62,63]. Furthermore, BC is known to be an important carrier of phosphorus into the ocean at the global scale, hence stimulating bacterioplankton and influencing microbial diversity [64]. However, the Humboldt current along the coast of Chile and Peru being already a thriving ecosystem, with an abundance of marine plants and animals, the input from forest fires through BC as evidenced in Figure 6, is not large enough to be expected to provide a significant change in the biodynamics of the area in terms of nitrogen, phosphorus, iron and silicon intake. Sulfuric acid (H_2SO_4) formed through SO_2 oxidation is highly soluble in water and tends to acidify the solution. Although ocean acidification is dominated by the dissolution of excess atmospheric CO_2 at the global scale, the deposition of sulfuric acid as observed in Figure 6 might locally and sporadically contribute to the decrease of ocean water pH and alter its alkalinity and inorganic carbon storage [65], with consequences on the ocean's viability for native plants and animal species. O_3 is known to have detrimental effects on plants yield when deposited on the leaves [6]. The large deposited quantities of this compound over land found by the model may thus suggest a potential loss in crop yields in 2017 although this hypothesis does not seem to have been investigated so far.

When looking at satellite images (Figures 7a and A3) one could arguably imagine that the observed coastal clouds near the fires would not have been formed without the CCN input stemming from those fires, as the rest of the region features mostly clear skies pointing towards conditions not favorable for cloud formation. The model says otherwise though, evidencing only a thickening of these clouds, but on the other hand seldom generates the clouds closest to the coastline that appear in the satellite images, while cloud cover far from the coast is adequately reproduced throughout the simulation in both the fire and control case. Several sources of bias in the simulation can explain the absence of coastal clouds (injection height of emissions, CCN activation parameterization, dry bias on humidity…). According to MODIS Terra cloud top height product (MOD06), the investigated coastal clouds were found mostly below 800 m above ground level. Our simulation consistently generates a CCN maximum number at around 500 m in the area of interest, although no clouds are formed near the coast due to unsaturated water vapor (relative humidity is around 0.95). Thus, the argument can be made that such coastal clouds indeed originate in the condensation of water vapor on fire-emitted nuclei, but small biases in the state of the atmosphere prevent them from being generated in the simulation. Furthermore, important processes are not yet taken into account in CHIMERE when in comes to biomass burning, such as the release of water vapor and heat by the fire, which can affect relative humidity. The representation of pyroconvection in coupled mode is also a development point of the model, as we would expect the phenomenon to lead to air masses convergence near ground-level hence affecting 10 m wind speed, which we showed is moderately changed and mostly due to the aerosol direct effect. Whether the observed coastal clouds would have existed without the fire event is thus not obvious, despite major implications in terms of meteorological feedback. In order to investigate this question on a climatological time scale, a long-term analysis based on clusters of MODIS cloud cover/height data with/without fire activity could be conducted, although it is out of the scope of this work.

5. Conclusions

This study investigated the impacts on air quality and meteorology of the early 2017 historic mega-fires in south-central Chile. Based on a chemistry-transport modeling approach with the fully coupled WRF-CHIMERE model, a set of two simulations was performed to assess the sensitivity of atmospheric variables to the occurrence of the afore-

mentioned fires. Surface and satellite observations were used to describe the event and assess the quality of the simulation. The pollutants plume originating from the fires spread across more than 2000 km, and up to 7 km above sea level on the vertical, causing AOD at 550 nm over the Pacific ocean off the coast of Chile to rise up to 4 on average for the most intense days. As a result, surface concentrations of pollutants in Santiago rose by +150% for $PM_{2.5}$ (+30 $\mu g/m^3$) and +50% for CO (+200 ppb), and a multiplication of AOD at all wavelengths by a factor 6 to 8 (+0.2 to +0.9 on average) was induced in the capital city, with a peak at 2.5 in AOD at 500 nm, explaining the serious health impacts of these fires recorded in the literature. Pollutants were also consequently deposited in large amounts over the land, the Andes cordillera and the Pacific ocean. Detrimental as well as fertilizing impacts can arise and should be further investigated. In addition to atmospheric composition and environmental impacts, the fire event showed a meteorological feedback with enhanced cloud formation over the ocean (aerosol indirect effect), as well as decreased surface radiation by up to 100 W/m^2, surface temperature by up to 1 K and mixing layer height by up to 100 m, on average, with disparities between land and ocean. Such modifications are substantial and should be taken into account in future projection scenarios, that foresee an increased frequency of biomass burning events of this magnitude in the region.

Author Contributions: As developers of CHIMERE, L.M. and S.M. supervised the chemistry-transport simulations and analyses of the results. R.L. performed the conceptualization, data analysis and model simulations and coordinated the writing of the paper with L.M. and S.M. All authors have read and agreed to the published version of the manuscript.

Funding: This research received no external funding.

Institutional Review Board Statement: Not applicable.

Informed Consent Statement: Not applicable.

Data Availability Statement: The WRF-CHIMERE online coupled model can be downloaded at https://www.lmd.polytechnique.fr/chimere/ (accessed on 1 October 2020).

Acknowledgments: The authors thankfully acknowledge the AERONET principal investigators of the Santiago Beauchef station, Roberto Rondanelli and Laura Gallardo, for establishing and maintaining the data used in this work. We acknowledge the NASA/MODAPS team for providing the MODIS products used in this study. We acknowledge the use of imagery from the NASA Worldview application (https://worldview.earthdata.nasa.gov (accessed on 1 October 2020)), part of the NASA Earth Observing System Data and Information System (EOSDIS). The authors acknowledge the AERIS data infrastructure (https://iasi.aeris-data.fr/ (accessed on 1 October 2020)) for providing access to the IASI data used in this study and ULB-LATMOS for the development of the retrieval algorithms. We also would like to thank the CALIOP team for providing the data obtained from the NASA Langley Research Center Atmospheric Science Data Center. Finally, the authors would like to acknowledge the work of the Editor and the three anonymous referees and thank them for their valuable comments and feedback.

Conflicts of Interest: The authors declare no conflict of interest.

Appendix A

Table A1. WRF and CHIMERE configurations.

WRF Configuration		CHIMERE Configuration	
Horizontal resolution	15 km	Horizontal resolution	15 km
Vertical levels	33	Vertical levels	30
Time step	30 s	Physical time step	15 min
Microphysics	Thompson aerosol-aware	Chemistry	MELCHIOR2
Boundary and surface layer	MYNN	Land Use	USGS
Land surface	Noah LSM	Horizontal Advection	Van Leer
Cumulus parameterization	Grell G3	Vertical Advection	Van Leer
Longwave/Shortwave radiation	RRTMG	Boundary Conditions	LMDz-INCA

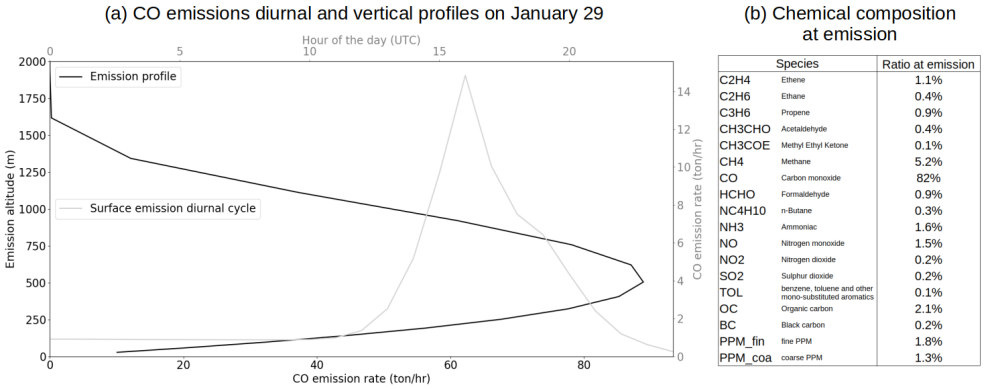

Figure A1. (**a**) CO emissions diurnal (gray line) and vertical (black line) profile on 29 January at the grid point of maximum intensity. (**b**) Molecular ratio of fire-emitted species at emission for the same grid point. Percentages give the number of molecules of each species over the total number of all molecules emitted by the fires.

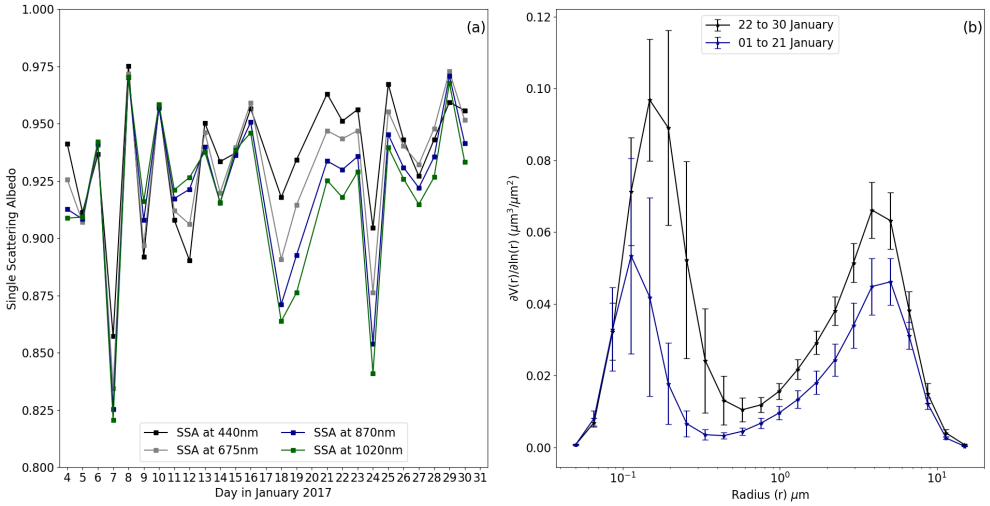

Figure A2. (**a**) SSA at 20:00 UTC recorded by AERONET (440, 675, 870 and 1020 nm) in January 2017. (**b**) Volume size distribution of aerosols before and during the fire events. Whiskers show one standard deviation. Observations from Santiago Beauchef AERONET station.

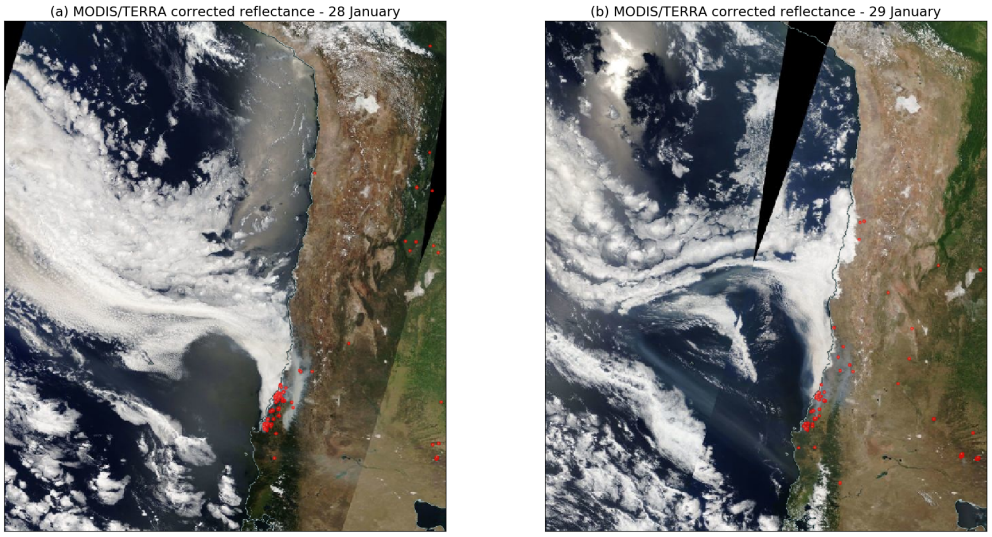

Figure A3. (**a**) Same as Figure 7a for 28 January. (**b**) Same as (**a**) for 29 January.

References

1. Seguel, R.J.; Mancilla, C.A.; Rondanelli, R.; Leiva, M.A.; Morales, R.G. Ozone distribution in the lower troposphere over complex terrain in Central Chile. *J. Geophys. Res. Atmos.* **2013**, *118*, 2966–2980. [CrossRef]
2. Gramsch, E.; Cereceda-Balic, F.; Oyola, P.; von Baer, D. Examination of pollution trends in Santiago de Chile with cluster analysis of PM10 and Ozone data. *Atmos. Environ.* **2006**, *40*, 5464–5475. [CrossRef]
3. de la Barrera, F.; Barraza, F.; Favier, P.; Ruiz, V.; Quense, J. Megafires in Chile 2017: Monitoring multiscale environmental impacts of burned ecosystems. *Sci. Total Environ.* **2018**, *637–638*, 1526–1536. [CrossRef] [PubMed]
4. Rubio, M.A.; Lissi, E.; Gramsch, E.; Garreaud, R.D. Effect of Nearby Forest Fires on Ground Level Ozone Concentrations in Santiago, Chile. *Atmosphere* **2015**, *6*, 1926–1938. [CrossRef]
5. Andreae, M.O. Emission of trace gases and aerosols from biomass burning—An updated assessment. *Atmos. Chem. Phys.* **2019**, *19*, 8523–8546. [CrossRef]
6. Hill, A.C.; Littlefield, N. Ozone. Effect on Apparent Photosynthesis, Rate of Transpiration, and Stomatal Closure in Plants. *Environ. Sci. Technol.* **1969**, *3*, 52–56. [CrossRef]
7. Lippmann, M. Health effects of tropospheric ozone. *Environ. Sci. Technol.* **1991**, *25*, 1954–1962. [CrossRef]
8. Ilabaca, M.; Olaeta, I.; Campos, E.; Villaire, J.; Tellez-Rojo, M.M.; Romieu, I. Association between Levels of Fine Particulate and Emergency Visits for Pneumonia and other Respiratory Illnesses among Children in Santiago, Chile. *J. Air Waste Manag.* **1999**, *49*, 154–163. [CrossRef]
9. Amdur, M.O. Health effects of air pollutants: Sulfuric acid, the old and the new. *Environ. Health Perspect* **1989**, *81*, 109–113. [CrossRef]
10. Corporación Nacional Forestal. CONAF. 2020. Available online: https://www.conaf.cl/incendios-forestales/incendios-forestales-en-chile/estadisticas-historicas/ (accessed on 1 October 2020).
11. Holz, A.; Paritsis, J.; Mundo, I.A.; Veblen, T.T.; Kitzberger, T.; Williamson, G.J.; Aráoz, E.; Bustos-Schindler, C.; González, M.E.; Grau, H.R.; et al. Southern Annular Mode drives multicentury wildfire activity in southern South America. *Proc. Natl. Acad. Sci. USA* **2017**, *114*, 9552–9557. [CrossRef]
12. McWethy, D.B.; Pauchard, A.; García, R.A.; Holz, A.; González, M.E.; Veblen, T.T.; Stahl, J.; Currey, B. Landscape drivers of recent fire activity (2001–2017) in south-central Chile. *PLoS ONE* **2018**, *13*, e0201195. [CrossRef]
13. Bowman, D.M.J.S.; Moreira-Muñoz, A.; Kolden, C.A.; Chávez, R.O.; Muñoz, A.A.; Salinas, F.; González-Reyes, Á.; Rocco, R.; de la Barrera, F.; Williamson, G.J.; et al. Human-environmental drivers and impacts of the globally extreme 2017 Chilean fires. *AMBIO* **2019**, *48*, 350–362. [CrossRef] [PubMed]
14. CR2. *The 2010–2015 Mega-Drought: A Lesson for the Future*; Technical Report; Center for Climate and Resilience Research: Santiago, Chile, 2015. Available online: http://www.cr2.cl/megasequia (accessed on 1 October 2020).
15. Garreaud, R.D.; Alvarez-Garreton, C.; Barichivich, J.; Boisier, J.P.; Christie, D.; Galleguillos, M.; LeQuesne, C.; McPhee, J.; Zambrano-Bigiarini, M. The 2010–2015 megadrought in central Chile: Impacts on regional hydroclimate and vegetation. *Hydrol. Earth Syst. Sci.* **2017**, *21*, 6307–6327. [CrossRef]
16. González, M.E.; Gómez-González, S.; Lara, A.; Garreaud, R.; Díaz-Hormazábal, I. The 2010–2015 Megadrought and its influence on the fire regime in central and south-central Chile. *Ecosphere* **2018**, *9*, 8. [CrossRef]
17. Castillo, M.; Plaza, A.; Garfias, R. A recent review of fire behavior and fire effects on native vegetation in Central Chile. *Glob. Ecol. Conserv.* **2020**, *24*, e01210. [CrossRef]
18. Sarricolea, P.; Serrano-Notivoli, R.; Fuentealba, M.; Hernández-Mora, M.; de la Barrera, F.; Smith, P.; Meseguer-Ruiz, O. Recent wildfires in Central Chile: Detecting links between burned areas and population exposure in the wildland urban interface. *Sci. Total Environ.* **2020**, *706*, 135894. [CrossRef]
19. Szopa, S.; Hauglustaine, D.A.; Ciais, P. Relative contributions of biomass burning emissions and atmospheric transport to carbon monoxide interannual variability. *Geophys. Res. Lett.* **2007**, *34*, L18810. [CrossRef]
20. Jacobson, M.Z. Effects of biomass burning on climate, accounting for heat and moisture fluxes, black and brown carbon, and cloud absorption effects. *J. Geophys. Res. Atmos.* **2014**, *119*, 8980–9002. [CrossRef]
21. Cussac, M.; Marécal, V.; Thouret, V.; Josse, B.; Sauvage, B. The impact of biomass burning on upper tropospheric carbon monoxide: A study using MOCAGE global model and IAGOS airborne data. *Atmos. Chem. Phys.* **2020**, *20*, 9393–9417. [CrossRef]
22. Lu, Z.; Sokolik, I.N. The Impacts of Smoke Emitted from Boreal Forest Wildfires on the High Latitude Radiative Energy Budget—A Case Study of the 2002 Yakutsk Wildfires. *Atmosphere* **2018**, *9*, 410. [CrossRef]
23. Vara-Vela, A.; de Fátima Andrade, M.; Zhang, Y.; Kumar, P.; Ynoue, R.Y.; Souto-Oliveira, C.E.; da Silva Lopes, F.J.; Landulfo, E. Modeling of atmospheric aerosol properties in the São Paulo Metropolitan Area: Impact of biomass burning. *J. Geophys. Res. Atmos.* **2018**, *123*, 9935–9956. [CrossRef]
24. Haslett, S.L.; Taylor, J.W.; Evans, M.; Morris, E.; Vogel, B.; Dajuma, A.; Brito, J.; Batenburg, A.M.; Borrmann, S.; Schneider, J.; et al. Remote biomass burning dominates southern West African air pollution during the monsoon. *Atmos. Chem. Phys.* **2019**, *19*, 15217–15234. [CrossRef]
25. Mailler, S.; Menut, L.; Khvorostyanov, D.; Valari, M.; Couvidat, F.; Siour, G.; Turquety, S.; Briant, R.; Tuccella, P.; Bessagnet, B.; et al. CHIMERE-2017: From urban to hemispheric chemistry-transport modeling. *Geosci. Model Dev.* **2017**, *10*, 2397–2423. [CrossRef]
26. Menut, L.; Flamant, C.; Turquety, S.; Deroubaix, A.; Chazette, P.; Meynadier, R. Impact of biomass burning on pollutant surface concentrations in megacities of the Gulf of Guinea. *Atmos. Chem. Phys.* **2018**, *18*, 2687–2707. [CrossRef]

27. Konovalov, I.B.; Beekmann, M.; Kuznetsova, I.N.; Yurova, A.; Zvyagintsev, A.M. Atmospheric impacts of the 2010 Russian wildfires: Integrating modelling and measurements of an extreme air pollution episode in the Moscow region. *Atmos. Chem. Phys.* **2011**, *11*, 10031–10056. [CrossRef]
28. Péré, J.C.; Bessagnet, B.; Mallet, M.; Waquet, F.; Chiapello, I.; Minvielle, F.; Pont, V.; Menut, L. Direct radiative effect of the Russian wildfires and its impact on air temperature and atmospheric dynamics during August 2010. *Atmos. Chem. Phys.* **2014**, *14*, 1999–2013. [CrossRef]
29. Konovalov, I.B.; Beekmann, M.; Berezin, E.V.; Petetin, H.; Mielonen, T.; Kuznetsova, I.N.; Andreae, M.O. The role of semi-volatile organic compounds in the mesoscale evolution of biomass burning aerosol: A modeling case study of the 2010 mega-fire event in Russia. *Atmos. Chem. Phys.* **2015**, *15*, 13269–13297. [CrossRef]
30. Hodzic, A.; Madronich, S.; Bohn, B.; Massie, S.; Menut, L.; Wiedinmyer, C. Wildfire particulate matter in Europe during summer 2003: Meso-scale modeling of smoke emissions, transport and radiative effects. *Atmos. Chem. Phys.* **2007**, *7*, 4043–4064. [CrossRef]
31. Majdi, M.; Turquety, S.; Sartelet, K.; Legorgeu, C.; Menut, L.; Kim, Y. Impact of wildfires on particulate matter in the Euro-Mediterranean in 2007: Sensitivity to some parameterizations of emissions in air quality models. *Atmos. Chem. Phys.* **2019**, *19*, 785–812. [CrossRef]
32. Majdi, M.; Kim, Y.; Turquety, S.; Sartelet, K. Impact of mixing state on aerosol optical properties during severe wildfires over the Euro-Mediterranean region. *Atmos. Environ.* **2020**, *220*, 117042. [CrossRef]
33. Malavelle, F.F.; Haywood, J.M.; Mercado, L.M.; Folberth, G.A.; Bellouin, N.; Sitch, S.; Artaxo, P. Studying the impact of biomass burning aerosol radiative and climate effects on the Amazon rainforest productivity with an Earth system model. *Atmos. Chem. Phys.* **2019**, *19*, 1301–1326. [CrossRef]
34. Amiri-Farahani, A.; Allen, R.J.; Li, K.F.; Nabat, P.; Westervelt, D.M. A La Niña-like climate response to south African biomass burning aerosol in CESM simulations. *J. Geophys. Res. Atmos.* **2020**, *125*. [CrossRef]
35. Mallet, M.; Solmon, F.; Nabat, P.; Elguindi, N.; Waquet, F.; Bouniol, D.; Sayer, A.M.; Meyer, K.; Roehrig, R.; Michou, M.; et al. Direct and semi-direct radiative forcing of biomass-burning aerosols over the southeast Atlantic (SEA) and its sensitivity to absorbing properties: A regional climate modeling study. *Atmos. Chem. Phys.* **2020**, *20*, 13191–13216. [CrossRef]
36. Holben, B.; Tanre, D.; Smirnov, A.; Eck, T.F.; Slutsker, I.; Abuhassan, N.; Newcomb, W.W.; Schafer, J.; Chatenet, B.; Lavenu, F.; et al. An emerging ground-based aerosol climatology: Aerosol optical depth from AERONET. *J. Geophys. Res.* **2001**, *106*, 12067–12097. [CrossRef]
37. Clerbaux, C. *Daily IASI/Metop-B ULB-LATMOS Carbon Monoxide (CO) L2 Product (Total Column)*; AERIS Data Infrastructure: San Jose, CA, USA, 2018. [CrossRef]
38. Bessagnet, B.; Menut, L.; Lapere, R.; Couvidat, F.; Jaffrezo, J.L.; Mailler, S.; Favez, O.; Pennel, R.; Siour, G. High Resolution Chemistry Transport Modeling with the On-line CHIMERE-WRF Model over the French Alps—Analysis of a Feedback of Surface Particulate Matter Concentrations on Mountainous Meteorology. *Atmosphere* **2020**, *11*, 565. [CrossRef]
39. Skamarock, W.C.; Klemp, J.B.; Dudhia, J.; Gill, D.O.; Barker, D.M.; Duda, M.G.; Huang, X.Y.; Wang, W.; Powers, J.G. *A Description of the Advanced Research WRF Version 3 (No. NCAR/TN-475+STR)*; University Corporation for Atmospheric Research: Boulder, CO, USA, 2008. [CrossRef]
40. Copernicus Atmosphere Monitoring Service. Global Fire Assimilation System. 2016. Available online: https://apps.ecmwf.int/datasets/data/cams-gfas/ (accessed on 1 October 2020).
41. Janssens-Maenhout, G.; Crippa, M.; Guizzardi, D.; Dentener, F.; Muntean, M.; Pouliot, G.; Keating, T.; Zhang, Q.; Kurokawa, J.; Wankmüller, R.; et al. HTAP_v2.2: A mosaic of regional and global emission grid maps for 2008 and 2010 to study hemispheric transport of air pollution. *Atmos. Chem. Phys.* **2015**, *15*, 11411–11432. [CrossRef]
42. Menut, L.; Bessagnet, B.; Khvorostyanov, D.; Beekmann, M.; Blond, N.; Colette, A.; Coll, I.; Curci, G.; Foret, G.; Hodzic, A.; et al. CHIMERE 2013: A model for regional atmospheric composition modelling. *Geosci. Model Dev.* **2013**, *6*, 981–1028. [CrossRef]
43. NCAR. *NCEP FNL Operational Model Global Tropospheric Analyses, Continuing from July 1999*; National Center for Atmospheric Research: Boulder, Colorado, 2000. [CrossRef]
44. Friedl, M.A.; Sulla-Menashe, D.; Tan, B.; Schneider, A.; Ramankutty, N.; Sibley, A.; Huang, X. MODIS Collection 5 Global Land Cover: Algorithm Refinements and Characterization of New Datasets, 2001–2012. Collection 5.1 IGBP Land Cover. 2010. Available online: http://lpdaac.usgs.gov (accessed on 1 October 2020).
45. Copernicus Climate Change Service (C3S). ERA5: Fifth Generation of ECMWF Atmospheric Reanalyses of the Global Climate. Copernicus Climate Change Service Climate Data Store (CDS). 2017. Available online: https://doi.org/http://doi.org/10.24381/cds.adbb2d47 (accessed on 1 October 2020).
46. Andela, N.; Kaiser, J.W.; van der Werf, G.R.; Wooster, M.J. New fire diurnal cycle characterizations to improve fire radiative energy assessments made from MODIS observations. *Atmos. Chem. Phys.* **2015**, *15*, 8831–8846. [CrossRef]
47. Sofiev, M.; Ermakova, T.; Vankevich, R. Evaluation of the smoke-injection height from wild-land fires using remote-sensing data. *Atmos. Chem. Phys.* **2012**, *12*, 1995–2006. [CrossRef]
48. Veira, A.; Kloster, S.; Wilkenskjeld, S.; Remy, S. Fire emission heights in the climate system—Part 1: Global plume height patterns simulated by ECHAM6-HAM2. *Atmos. Chem. Phys.* **2015**, *15*, 7155–7171. [CrossRef]
49. Beegum, S.N.; Tuomiranta, A.; Gherboudj, I.; Flemming, J.; Ghedira, H. Simulation of aerosol deposition flux over the Arabian Peninsula with CHIMERE-2017: Sensitivity to different dry deposition schemes. *Atmos. Res.* **2020**, *241*, 104949. [CrossRef]

50. Bahadur, R.; Praveen, P.S.; Xu, Y.; Ramanathan, V. Solar absorption by elemental and brown carbon determined from spectral observations. *Proc. Natl. Acad. Sci. USA* **2012**, *109*, 17366–17371. [CrossRef] [PubMed]
51. Winker, D.M.; Pelon, J.; Coakley, J.A., Jr.; Ackerman, S.A.; Charlson, R.J.; Colarco, P.R.; Flamant, P.; Fu, Q.; Hoff, R.M.; Kittaka, C.; et al. The CALIPSO mission: A global 3D view of aerosols and clouds. *Bull. Am. Meteorol. Soc.* **2010**, *91*, 1211–1230. [CrossRef]
52. Omar, A.; Winker, D.M.; Vaughan, M.A.; Hu, Y.; Trepte, C.R.; Ferrare, R.A.; Lee, K.P.; Hostetler, C.A.; Kittaka, C.; Rogers, R.R.; et al. The CALIPSO Automated Aerosol Classification and Lidar Ratio Selection Algorithm. *J. Atmos. Ocean. Tech.* **2009**, *26*, 1994–2014. [CrossRef]
53. Chen, Z.; Torres, O.; McCormick, M.P.; Smith, W.; Ahn, C. Comparative study of aerosol and cloud detected by CALIPSO and OMI. *Atmos. Environ.* **2012**, *51*, 187–195. [CrossRef]
54. Winker, D.M.; Tackett, J.L.; Getzewich, B.J.; Liu, Z.; Vaughan, M.A.; Rogers, R.R. The global 3-D distribution of tropospheric aerosols as characterized by CALIOP. *Atmos. Chem. Phys.* **2013**, *13*, 3345–3361. [CrossRef]
55. Fiedler, V.; Arnold, F.; Ludmann, S.; Minikin, A.; Hamburger, T.; Pirjola, L.; Dörnbrack, A.; Schlager, H. African biomass burning plumes over the Atlantic: Aircraft based measurements and implications for H_2SO_4 and HNO_3 mediated smoke particle activation. *Atmos. Chem. Phys.* **2011**, *11*, 3211–3225. [CrossRef]
56. Seinfeld, J.H.; Pandis, S.N. *Atmospheric Chemistry and Physics: From Air Pollution to Climate Change*, 2nd ed.; John Wiley & Sons: Hoboken, NJ, USA, 2006.
57. IPCC. *Climate Change 2013: The Physical Science Basis. Contribution of Working Group I to the Fifth Assessment Report of the Intergovernmental Panel on Climate Change*; Stocker, T.F., Qin, D., Plattner, G.-K., Tignor, M., Allen, S.K., Boschung, J., Nauels, A., Xia, Y., Bex, V., Midgley, P.M., Eds.; Cambridge University Press: Cambridge, UK; New York, NY, USA, 2013.
58. Boucher, O.; Randall, D.; Artaxo, P.; Bretherton, C.; Feingold, G.; Forster, P.; Kerminen, V.M.; Kondo, Y.; Liao, H.; Lohmann, U.; et al. Chapter: Clouds and Aerosols. In *Climate Change 2013: The Physical Science Basis. Contribution of Working Group I to the Fifth Assessment Report of the Intergovernmental Panel on Climate Change*; Stocker, T.F., Qin, D., Plattner, G.-K., Tignor, M., Allen, S.K., Boschung, J., Nauels, A., Xia, Y., Bex, V., Midgley, P.M., Eds.; Cambridge University Press: Cambridge, UK; New York, NY, USA, 2013.
59. Whiteman, D.C. *Mountain Meteorology: Fundamentals and Applications*; Oxford University Press: Oxford, UK; New York, NY, USA, 2000. [CrossRef]
60. Shrestha, G.; Traina, S.J.; Swanston, C.W. Black Carbon's Properties and Role in the Environment: A Comprehensive Review. *Sustainability* **2010**, *2*, 294–320. [CrossRef]
61. Anda, A.; Illes, B. Impact of Simulated Airborne Soot on Maize Growth and Development. *J. Environ. Prot.* **2012**, *3*, 773–781. [CrossRef]
62. Zhang, Y.; Kang, S.; Cong, Z.; Schmale, J.; Sprenger, M.; Li, C.; Yang, W.; Gao, T.; Sillanpää, M.; Li, X.; et al. Light-absorbing impurities enhance glacier albedo reduction in the southeastern Tibetan plateau. *J. Geophys. Res. Atmos.* **2017**, *122*, 6915–6933. [CrossRef]
63. Kang, S.; Zhang, Y.; Qian, Y.; Wang, H. A review of black carbon in snow and ice and its impact on the cryosphere. *Earth-Sci. Rev.* **2020**, *210*, 103346. [CrossRef]
64. Weinbauer, M.G.; Guinot, B.; Migon, C.; Malfatti, F.; Mari, X. Skyfall-neglected roles of volcano ash and black carbon rich aerosols for microbial plankton in the ocean. *J. Plankton Res.* **2017**, *39*, 187–198. [CrossRef]
65. Doney, S.C.; Mahowald, N.; Lima, I.; Feely, R.A.; Mackenzie, F.T.; Lamarque, J.F.; Rasch, P.J. Impact of anthropogenic atmospheric nitrogen and sulfur deposition on ocean acidification and the inorganic carbon system. *Proc. Natl. Acad. Sci. USA* **2007**, *104*, 14580–14585. [CrossRef] [PubMed]